Heliyon 10 (2024) e36206

Contents lists available at ScienceDirect

Heliyon

journal homepage: www.cell.com/heliyon

Research article

Microwave-assisted solvothermal synthesis of nanostructured Ga-Doped $Li_7La_3Zr_2O_{12}$ solid electrolyte with enhanced densification and Li-ion conductivity

Seong-Jun Jo [a,b,1], Young Gyu Jeon [a,b,1], Dong-Kyu Kim [a,b,1], Sang Yeop Hwang [a,b], Byeong-Heon Lee [a,b], Chea Yun Kang [a,b], Seung-Hwan Lee [a,b], Sung-Hwan Lim [a,b], R. Vasant Kumar [c], Yu-Jin Han [d,**], Kwang-Bum Kim [e,***], Hyun-Kyung Kim [a,b,*]

[a] Department of Battery Convergence Engineering, Kangwon National University, 1 Kangwondaehak-gil, Chuncheon, 24341, Republic of Korea
[b] Interdisciplinary Program in Advanced Functional Materials and Devices Development, Kangwon National University, Chuncheon, 24341, Republic of Korea
[c] Department of Materials Science and Metallurgy, University of Cambridge, 27 Charles Babbage Road, Cambridge, CB3 0FS, UK
[d] Ulsan Advanced Energy Technology R&D Center, Korea Institute of Energy Research, Ulsan, 44776, Republic of Korea
[e] Department of Materials Science and Engineering, Yonsei University, 134 Shinchon-dong, Seodaemoon-gu, Seoul, 120-749, Republic of Korea

ARTICLE INFO

Keywords:
Li-ion solid electrolytes
Garnet-type $Li_7La_3Zr_2O_{12}$
Microwave-assisted solvothermal synthesis
Solid-state batteries

ABSTRACT

Garnet-type $Li_7La_3Zr_2O_{12}$ (LLZO) Li-ion solid electrolytes are promising candidates for safe, next-generation solid-state batteries. In this study, we synthesize Ga-doped LLZO (Ga–LLZO) electrolytes using a microwave-assisted solvothermal method followed by low-temperature heat treatment. The nanostructured precursor (<50 nm) produced by the microwave-assisted solvothermal process has a high surface energy, facilitating the reaction for preparing garnet-type Ga–LLZO powders (<800 nm) within a short time (<5 h) at a low calcination temperature (<700 °C). Additionally, the calcined nanostructured Ga–LLZO powder can be sintered to produce a high-density pellet with minimized grain boundaries under moderate sintering conditions (temperature: 1150 °C, duration: 10 h). The optimal doping concentration was determined to be 0.4 mol% Ga, which resulted significantly increased the ionic conductivity (1.04×10^{-3} S cm^{-1} at 25 °C) and stabilized the cycling performance over 1700 h at 0.4 mA cm^{-2}. This approach demonstrates the potential to synthesize oxide-type solid electrolyte materials with improved properties for solid-state batteries.

Abbreviations: EV, electric vehicle; LIB, Li-ion battery; XRD, X-ray diffraction; SEM, scanning electron microscopy; EDS, energy-dispersive X-ray spectroscopy; EIS, electrochemical impedance spectroscopy; MW, microwave; SG, sol-gel.

* Corresponding author. Department of Battery Convergence Engineering, Kangwon National University, 1 Kangwondaehak-gil, Chuncheon, 24341, Republic of Korea.
** Corresponding author. Ulsan Advanced Energy Technology R&D Center, Korea Institute of Energy Research, Ulsan, 44776, Republic of Korea.
*** Corresponding author. Department of Materials Science and Engineering, Yonsei University, 134 Shinchon-dong, Seodaemoon-gu, Seoul, 120-749, Republic of Korea.
E-mail addresses: han@kier.re.kr (Y.-J. Han), kbkim@yonsei.ac.kr (K.-B. Kim), hkk@kangwon.ac.kr (H.-K. Kim).
[1] These authors contributed equally to this work.

https://doi.org/10.1016/j.heliyon.2024.e36206
Received 3 July 2024; Received in revised form 7 August 2024; Accepted 12 August 2024
Available online 20 August 2024

1. Introduction

Spurred by the recent global energy crisis and environmental concerns, several countries have started producing electric vehicles (EVs). Li-ion batteries (LIBs) have been adopted for EVs owing to their high stability and energy densities [1–3]. However, LIBs with flammable organic liquid electrolytes exhibit safety issues such as combustion and explosion [4–6], which can be mitigated by using highly stable cathode materials, electrolytes with a wide voltage window, or solid electrolytes [7,8]. Especially, solid electrolytes can help address the safety issues of conventional LIBs by eliminating the risks associated with organic liquid electrolytes. Consequently, research and application of solid electrolytes in LIBs have rapidly surged in recent years.

Inorganic solid-state electrolytes, such as sulfides and oxides, offer wide electrochemical potential windows and high mechanical strengths compared with organic liquid electrolytes. Owing to these features, metallic Li (3860 mAh g^{-1}) can be used as an anode and high-voltage cathode (~5 V), resulting in a high energy density and long cycle life [5,9]. Sulfide electrolytes provide high Li-ion conductivity due to their mechanical flexibility; however, they exhibit poor chemical stability and are sensitivity to moisture, which can lead to H_2S gas generation [9,10]. In contrast, oxide electrolytes exhibit good chemical stability, high crystallinity, and excellent mechanical properties, effectively suppressing Li dendrite formation [11,12]. Oxide electrolytes, such as perovskites ($Li_{3x}La_{2/3x}TiO_3$, LLTO), NASICON ($Li_{1+x}Al_xTi_{2-x}(PO_4)_3$, LATP), and garnet ($Li_7La_3Zr_2O_{12}$, LLZO) are widely studied owing to their superior properties [13–16]. However, Ti-containing oxides like LLTO or LATP are prone to reduction and can easily undergo mechanical and thermal damage [17–20].

LLZO exhibits stability against oxygen in air, high chemical stability when in contact with both a Li-metal anode and high-voltage cathode material, a high Li-ion conductivity (>10^{-4} S cm^{-1} at room temperature, 25 °C), and a wide electrochemical window (>5 V vs. Li/Li^+) [2,15,16]. LLZO crystallizes in either tetragonal or cubic symmetry, with the cubic phase exhibiting a higher Li-ion conductivity owing to its disordered Li-ion distribution [21]. Thus, cubic-phase LLZO is more suitable than its tetragonal counterpart for use as a solid electrolyte. Aliovalent doping with elements such as Al, Ga, Ca, Sr, Ta, Nb, and F stabilizes the cubic phase and enhances the Li-ion conductivity of LLZO [22–32]. Studies have shown that Ga^{3+} doping creates Li^+ vacancies that enhance Li^+ migration, whereas Al^{3+} can hinder this process by occupying Li^+ sites [22,23]. Ga^{3+}, which is larger than Al^{3+}, causes lattice distortion, thereby opening multiple Li^+ migration routes and improving the Li-ion conductivity of Ga-doped LLZO (Ga–LLZO) [23].

Ga–LLZO with a complex garnet structure is typically synthesized using conventional sol–gel (SG) or solid-state methods, wherein the powders are usually calcined and sintered at temperatures over 800 and 1200 °C, respectively [33–35]. These conventional approaches generally require high calcination/sintered temperatures and long heating durations. Under such conditions, the highly reactive Li species can become volatile and lead to the formation of pyrochlore phases, which can reduce the Li-ion conductivity. One potential solution to address these issues is the use of nanostructured powders [36,37], which provide large interfacial and surface areas, thus enabling densification and maximizing grain coarsening during sintering. However, traditional synthesis methods such as the SG process experience considerable heat transfer owing to external heating, leading to significant temperature gradients within the reaction vessel. This can lead to heterogeneous particle size and extend the synthesis time, ultimately resulting in larger particles because of continuous nucleation. Therefore, new approaches for synthesizing nanostructured LLZO are required to balance the sintering conditions, pellet density, and Li loss.

Microwave (MW)-assisted solvothermal methods have been widely employed to fabricate nanoparticles owing to their unique ability to rapidly and homogeneously heat precursor materials [38]. MWs, which have frequencies between 300 and 300,000 MHz, penetrate the solution, allowing for uniform heating. Consequently, they minimize the temperature gradients within the vessel, promoting consistent and rapid nucleation [39]. These features enable the formation of nanoparticles with narrow size distributions, making MW-assisted solvothermal synthesis a promising approach for producing nanoparticles with the desired properties [40].

Herein, we introduce a facile approach to synthesize high-ionic-conductivity Ga–LLZO using a MW-assisted solvothermal process and subsequent low-temperature heat treatments. In this study, we determined the optimal Ga doping amount to maximize the Li-ion conductivity. The MW method efficiently produced nanostructured 0.4 Ga–LLZO precursors (<50 nm) and powders (<800 nm) withing a short reaction time. The nanostructured 0.4 Ga–LLZO powder, whose surface area increased under low-temperature and short-time calcination conditions (700 °C, 5 h), was sintered to produce high-density pellets with minimized grain boundaries, which resulted in improved Li-ion conductivity (1.04×10^{-3} S cm^{-1} at 25 °C). Stability testing showed over 1700 h of stable cycling at 0.4 mA cm^{-2}, suggesting potential application of the synthesized Ga–LLZO in stable, efficient solid-state batteries.

2. Materials and methods

2.1. MW-assisted solvothermal synthesis of xGa–LLZO (MW xGa–LLZO)

The MW xGa–LLZO (x: 0–0.45 mol%) ceramic samples were fabricated using the MW-assisted solvothermal method. Stoichiometric amounts of $Ga(NO_3)_3$ (Thermo Scientific, 99.9998 % trace metal basis), $La(NO_3)_3$ (Aldrich, 99.9 % trace metal basis), and $ZrO(NO_3)_2$ (Aldrich, 99 %) combined with excessive LiOH (20 %) were dissolved in diethylene glycol (Sigma-Aldrich, ReagentPlus®, 99 %) to provide metal ions, and citric acid (Alfa-Aesar, anhydrous, 99.5+%) was introduced as a chelating agent. Excessive LiOH (20 %) was added to compensate for Li loss during sintering. The mixture was stirred at room temperature (25 °C) for 5 h to obtain a homogeneous solution. The obtained solution was loaded into a sealed Teflon vessel and placed in an MW system (MARS-5, CEM Corporation), where it was heated to 250 °C and maintained at that temperature for 10 min. The solution was then allowed to cool naturally to room temperature. The precipitates were centrifuged (1580R, LABOGENE) at 10,000 rpm for 1 h using a laboratory centrifuge and then dried at 250 °C for 2 h to remove the residual solvent. The precursor was calcined at 700 °C in air for 5 h to crystallize the MW

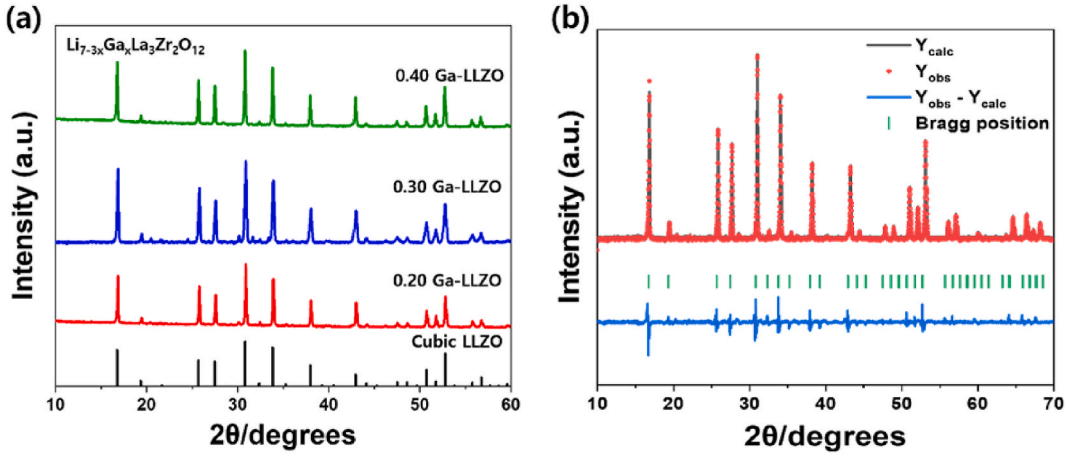

Fig. 1. (a) XRD patterns of MW 0.2–0.4 Ga–LLZO; (b) Rietveld refinement of the XRD data for MW 0.4 Ga–LLZO.

xGa–LLZO structure. Finally, the powders were pressed into 12-mm-diameter pellets in a hydraulic press under a pressure of 3000 psi. The resulting pellets were sintered at 1150 °C for 10 h. To avoid Li volatilization and Al^{3+} contamination, the MW xGa–LLZO pellets were covered with their respective mother powders in an alumina crucible, which were the same as those used to prepare the MW xGa–LLZO powders.

2.2. SG synthesis of 0.4 Ga–LLZO (SG 0.4 Ga–LLZO)

The SG 0.4 Ga–LLZO ceramic samples were fabricated using the SG method. Stoichiometric amounts of $Ga(NO_3)_3$ (Thermo Scientific, 99.9998 % trace metal basis), $La(NO_3)_3$ (Aldrich, 99.9 % trace metal basis), and $ZrO(NO_3)_2$ (Aldrich, 99 %), with an excess of $LiNO_3$ (20 %), were dissolved in deionized water to provide metal ions, and citric acid (Alfa-Aesar, anhydrous, 99.5+%) was introduced as a chelating agent. An excessive amount of $LiNO_3$ (20 %) was added to compensate for Li loss during sintering. To adjust the pH of the prepared solution to 7, $NH_3{\cdot}H_2O$ (ACROS ORGANICS, 28–30 % solution in water) was added. The mixture was then stirred for 12 h at room temperature to obtain a homogeneous solution, which was then gelled by drying at 100 °C for 12 h, followed by drying at 250 °C for 2 h to obtain a precursor. The precursor was calcined at 700 °C in air for 5 h to crystallize the structure. Finally, the SG 0.4 Ga–LLZO powder was pressed into 12-mm-diameter pellets in a hydraulic press under a pressure of 3000 psi. The resulting pellets were sintered at 1150 °C for 10 h. To avoid Li volatilization and Al^{3+} contamination, the SG 0.4 Ga–LLZO pellets were covered with their respective mother powders in an alumina crucible. The mother powders used were the same as those used to prepare the SG 0.4 Ga–LLZO powders.

2.3. Material characterization

X-ray diffraction (XRD; PANalytical, X'Pert PRO MPD) was used to examine the crystalline structures of the calcined Ga–LLZO powders with Cu-Kα radiation ($\lambda = 1.5406$ Å) from 2θ values of 10°–60° with a step width of 0.013°. Scanning electron microscopy (SEM; JEOL, JSM-7900F) was used to observe the grain size, morphology, and elemental distribution of the powder samples. Particle size analysis (Anton Paar, PSA 1090 L) was performed to compare the particle size and distribution of the powders synthesized using the MW and SG methods. The surface area was estimated by obtaining N_2 adsorption–desorption isotherms and applying the Brunauer–Emmett–Teller method (Microtrac MRB, Belsorp Max G). The powder samples were then pressed into pellets. SEM coupled with energy-dispersive X-ray spectroscopy (SEM–EDS) analyses were to evaluate the cross-sectional morphology of these pellet samples. The SEM–EDS samples were prepared using the ion-milling method to compare the grain-boundary distribution of the pellets prepared using the MW and SG methods. The pellets were mounted in a brass tube using G1 epoxy and a hardener to prepare the ion-milled samples. The density of the ceramic pellets was measured using the Archimedes method with anhydrous ethanol as the immersion medium, as LLZO can absorb water, making it an unsuitable medium. The density of Ga–LLZO was determined from its mass and volume, and its relative density values were calculated by dividing the measured density by the theoretical density of LLZO (~5.1 g cm^{-3}) [41]. Next, samples with a thickness of 75 μm were fabricated by grinding the pellet using sandpapers with progressively finer grits (400, 600, 800, and 1200 grit). The ground samples were polished using a polishing cloth and diamond suspension. The final polishing step was performed using a 2 keV beam, with dual beam conditions of 3° upward for the left and right guns, for 15 min; this final polishing step was performed using a precision ion polishing system (Gatan, Model 691).

2.4. Electrochemical measurements

An alternating-current impedance tester (Biologic, SP-200) was used to measure the Li-ion conductivity indirectly at frequencies

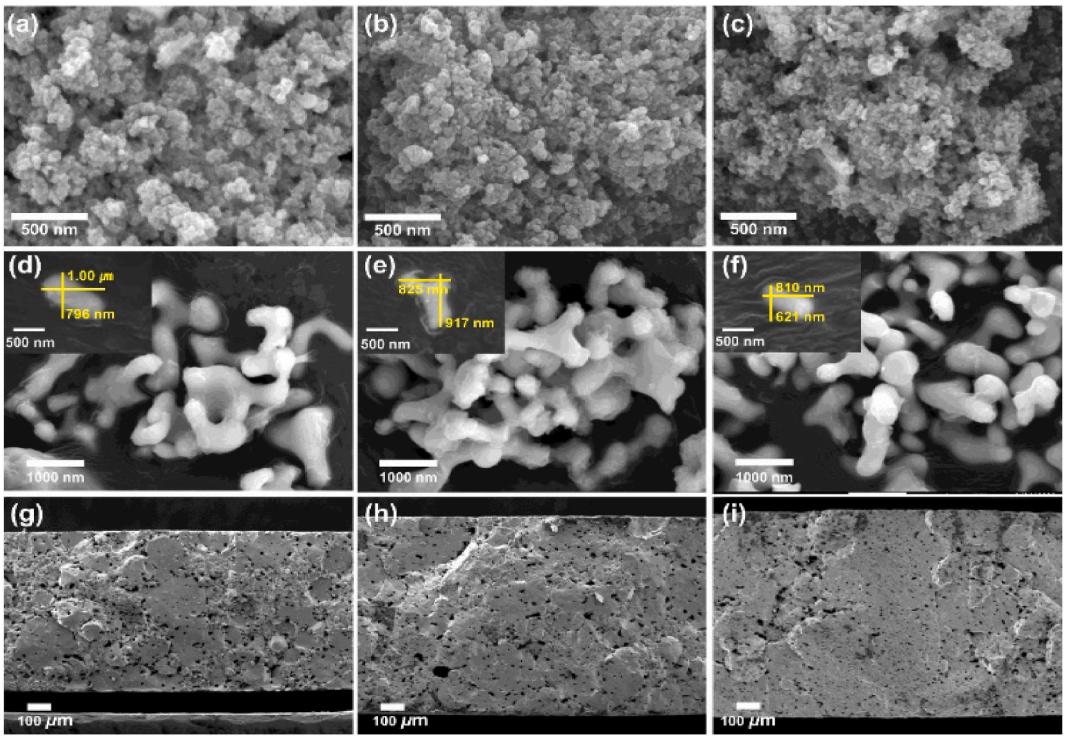

Fig. 2. SEM images of MW xGa–LLZO. Top row, precursor; middle row, powder; bottom row, fracture surface of the corresponding pellet. (a), (d), and (g) MW 0.2 Ga–LLZO; (b), (e), and (h) MW 0.3 Ga–LLZO; and (c), (f), and (i) MW 0.4 Ga–LLZO.

ranging from 7 MHz to 1 Hz, an amplitude of 7 mV, and temperatures ranging from 25 to 80 °C in the temperature chamber. The diameter and thickness of the samples were ~10 and ~1 mm, respectively. Prior to the Li-ion conductivity measurements, an Au/ prepared Ga–LLZO/Au cell was prepared by sputtering a layer of Au onto both sides of the pellet samples, which were polished with sandpaper. The samples were then annealed for 1 h at the required temperature before each measurement. The Li-ion conductivity of the Ga–LLZO pellets was obtained from their corresponding Nyquist plots using the Z-Fit analysis tool present in the Biologic BT-lab software. The activation energy was calculated using the Arrhenius equation.

A Li/MW 0.4 Ga–LLZO/Li cell was also prepared; two pieces of metallic Li were attached to both sides of the pellet samples, which were then converted into a CR2032 coin cell configuration inside a glovebox filled with Ar. The cycling performance of the Li symmetric cell was measured using a battery tester (Neware, BTS-4008-5V50mA). The Li symmetric cell was subjected to a galvanostatic cycling test at 0.4 mA cm^{-2} for 1 h per cycle at 25 °C.

3. Results and discussion

3.1. Powder and sintered pellet morphology

Ga–LLZO powders were prepared with various Ga contents using an MW-assisted solvothermal method and via calcination (<700 °C in 5 h); these samples are hereafter labeled as "MW xGa–LLZO," where x = 0.2–0.45. The XRD patterns of the calcined MW 0.2–0.4 Ga–LLZO powders are presented in Fig. 1a [42–45], confirming that a cubic phase is formed when the Ga content in LLZO is > 0.2 mol% [46,47]. As shown in Fig. S1, the XRD pattern of MW 0 Ga–LLZO exhibits the characteristic peaks of the tetragonal phase, and below a Ga content of 0.2 mol%, the characteristic peaks of the impurity phase $La_2Zr_2O_7$ (LZO) appear [48,49]. When the Ga content is low, the cubic phase of LLZO may be relatively unstable, which can lead to the formation of the tetragonal phase. Moreover, it is important to consider that the Li source and LZO may not fully react at the synthesis temperature of 700 °C. Both of these factors can significantly impact the overall stability and performance of the synthesized materials. Additionally, when the Ga content in LLZO exceeds 0.4 mol% (MW 0.45 Ga–LLZO), the LZO impurity phase reappears. Ga has limited solubility in LLZO; therefore, at higher Ga concentrations, an excess of Ga may increase the loss of Li, also resulting in the formation of the LZO impurity phase [50]. The Rietveld refinement of the XRD data (Fig. 1b) suggests that MW 0.4 Ga–LLZO can be well indexed to the cubic garnet phase, indicating that Ga-ion substitution can stabilize this phase. The refinement yielded a weighted profile residual (R_{wp}) of 10.2 %, an expected profile residual (R_{exp}) of 3.13 %, and a chi-squared (χ^2) value of 3.26. These values indicate a satisfactory fit between the observed and calculated XRD patterns, suggesting that this phase structure appropriately describes the material.

The SEM images presented in Fig. 2 reveal the morphologies of the MW 0.2–0.4 Ga–LLZO precursors, calcined powders, and

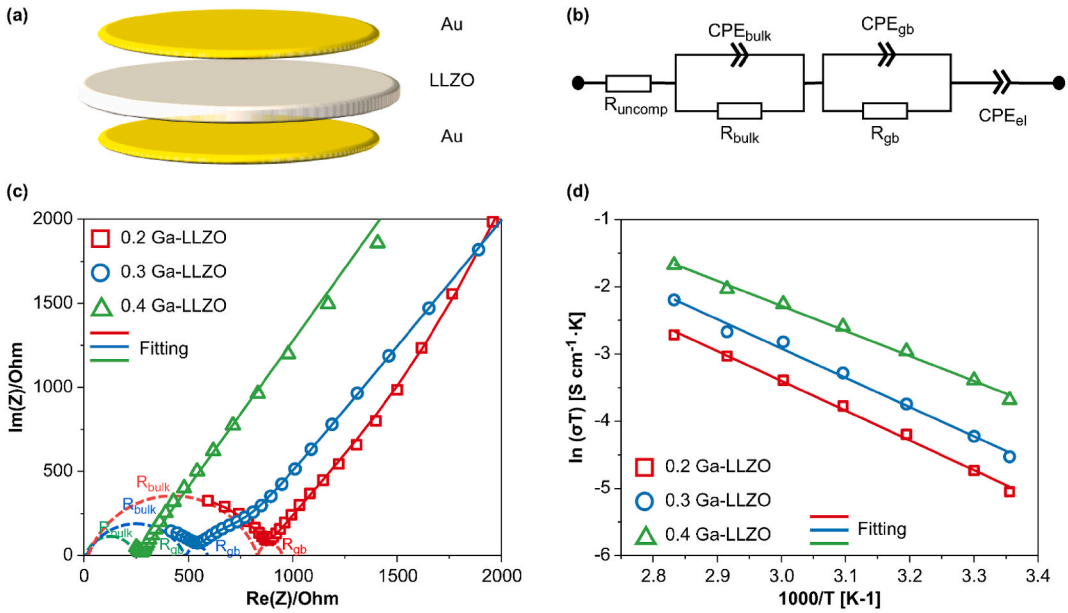

Fig. 3. (a) Schematic of the Au/LLZO/Au cell fabricated for EIS measurements; (b) equivalent circuit for fitting the EIS data of the Au/MW 0.2–0.4 Ga–LLZO/Au cell; (c) Nyquist plots of the MW 0.2–0.4 Ga–LLZO pellets; (d) Arrhenius plots of the MW 0.2–0.4 Ga–LLZO pellets.

Table 1
Lattice parameters, total conductivity, and activation energy of MW 0.2–0.4 Ga–LLZO.

Li:La:Zr:Ga	Lattice parameter (Å)	Li-ion conductivity (S cm^{-1})	Activation energy (eV)
6.4:3:2:0.2	12.9934	1.91×10^{-4}	0.38
6.1:3:2:0.3	12.9915	3.84×10^{-4}	0.38
5.8:3:2:0.4	12.9902	1.04×10^{-3}	0.32

sintered pellets. Fig. 2a–c demonstrates the uniform morphology of the as-synthesized MW 0.2–0.4 Ga–LLZO precursors, which are approximately 50 nm in size. This nanostructure can be attributed to the advantages of the MW-assisted solvothermal method. The SEM images presented in Fig. 2d–f reveal that the post-calcination powder particle size decreases from >1 μm to <800 nm with the increasing Ga content. This decrease is attributed to the reduction in surface energy caused by Ga doping [51]. As shown in Fig. 2g–i, the subsequent sintering process caused grain coarsening in the nanostructured LLZO precursor, which reduced the number of grain boundaries within the resulting pellet. SEM images of the powders with different Ga contents (MW 0–0.45 Ga–LLZO) after calcination are shown in Fig. S2, and the corresponding pellets with grain coarsening after sintering are shown in Fig. S3.

3.2. *Electrochemical properties*

Electrochemical impedance spectroscopy (EIS) was performed to investigate the effect of minimized grain boundaries on the electrical resistance and Li-ion conductivity of the pellet at 25 °C. An Au/MW 0.2–0.4 Ga–LLZO/Au symmetrical cell was fabricated to measure the pellet resistance; the corresponding results are shown in Fig. 3a.

The obtained EIS data were fitted using an equivalent circuit model (Fig. 3b). Fig. 3c presents the Nyquist plots derived from the EIS analysis, revealing the resistance and Li-ion conductivity of the pellets as a function of the Ga content. The Nyquist plot exhibits a semicircle at high frequencies, a semicircle at mid-frequencies, and a tail at low frequencies. The semicircle at high frequencies indicates bulk resistance (R_b), whereas that at mid-frequencies indicates intergranular resistance (R_{gb}) [52–54]. These results confirm that both the bulk and grain-boundary resistances gradually decrease with an increase in the Ga content, and this result is attributed to the reduction in the number of grain boundaries and densification of the pellets due to grain coarsening. The value of the *x*-intercept of the semicircle at the mid-frequency corresponds to the total resistance. The determined total resistance values of MW 0.2 Ga–LLZO, MW 0.3 Ga–LLZO, and MW 0.4 Ga–LLZO are 1114.5, 679.2, and 265 Ω, respectively. The Li-ion conductivity (σ) of the pellets is calculated using Equation (1) [55]:

$$\sigma = \frac{L}{R \times S}, \tag{1}$$

where *R*, *L*, and *A* represent the resistance, thickness of the pellet, and electrode area, respectively. The calculated Li-ion conductivities

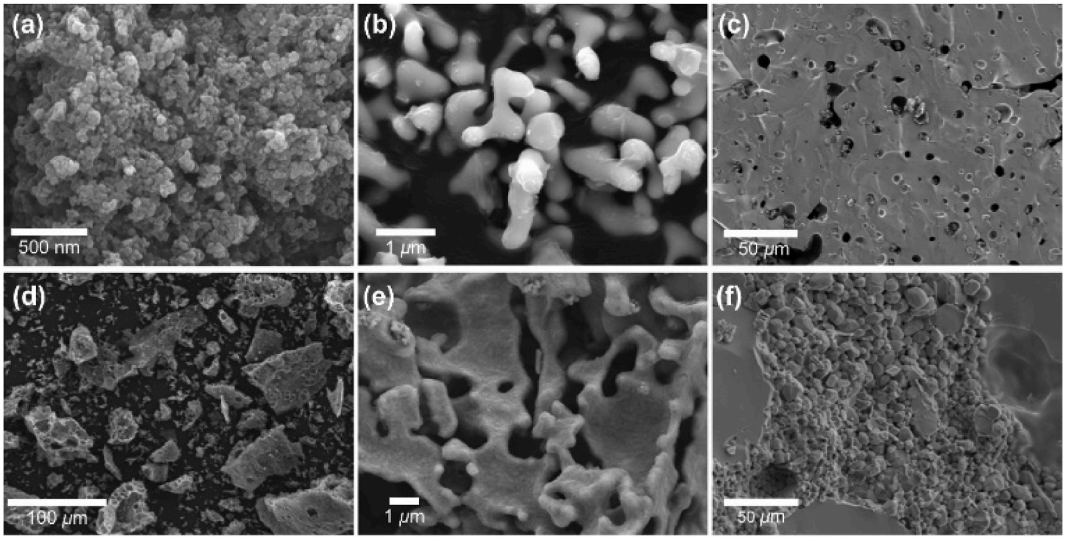

Fig. 4. SEM images of the MW 0.4 Ga–LLZO (a) precursor, (b) powder, (c) pellet fracture surface, and SG 0.4 Ga–LLZO (d) precursor, (e) powder, and (f) pellet fracture surface.

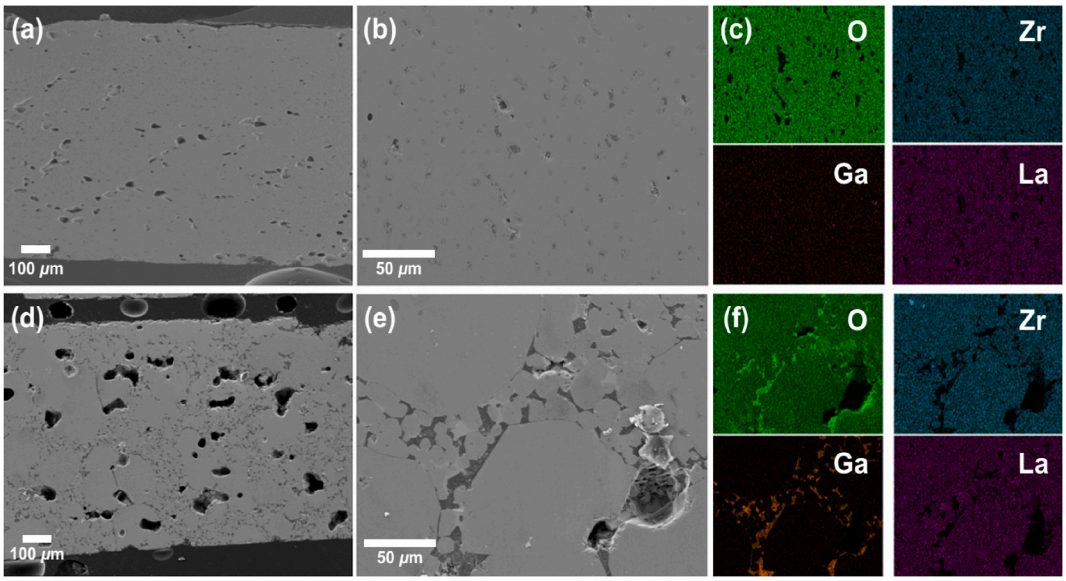

Fig. 5. SEM images of the ion-milled pellet surfaces: (a, b) MW 0.4 Ga–LLZO and (d, e) SG 0.4 Ga–LLZO. EDS mapping data of (c) MW 0.4 Ga–LLZO and (f) SG 0.4 Ga–LLZO.

of MW 0.2 Ga–LLZO, MW 0.3 Ga–LLZO, and MW 0.4 Ga–LLZO are 1.91×10^{-4}, 3.84×10^{-4}, and 1.04×10^{-3} S cm^{-1}, respectively (Table 1). Conversely, small grains may produce the lowest Li-ion conductivity. Combined with the morphology analysis findings, these results suggest that the observed decrease in the number of grain boundaries in MW 0.4 Ga–LLZO corresponds to a decrease in the pellet resistance, which enhances the potential for producing pellets with a high Li-ion conductivity.

However, MW 0.45 Ga–LLZO exhibits abnormal grain coarsening, which increases its resistance while decreasing its Li-ion conductivity, as shown by the Nyquist plots in Fig. S4. These results suggest that tiny grains can result in abnormal grain coarsening, a high resistance, and the lowest Li-ion conductivity after sintering. These findings confirm that MW 0.4 Ga–LLZO with the smallest grains can achieve the highest Li-ion conductivity. EIS analysis was also conducted at various temperatures (from 25 to 80 °C) to investigate the effect of temperature on the Li-ion conductivity of Ga–LLZO. The Li-ion conductivities of the LLZO pellets, with different Ga contents, measured at various temperatures are plotted on an Arrhenius plot in Fig. 3d. The activation energy (E_a) of the pellet is calculated using Equation (2) [55].

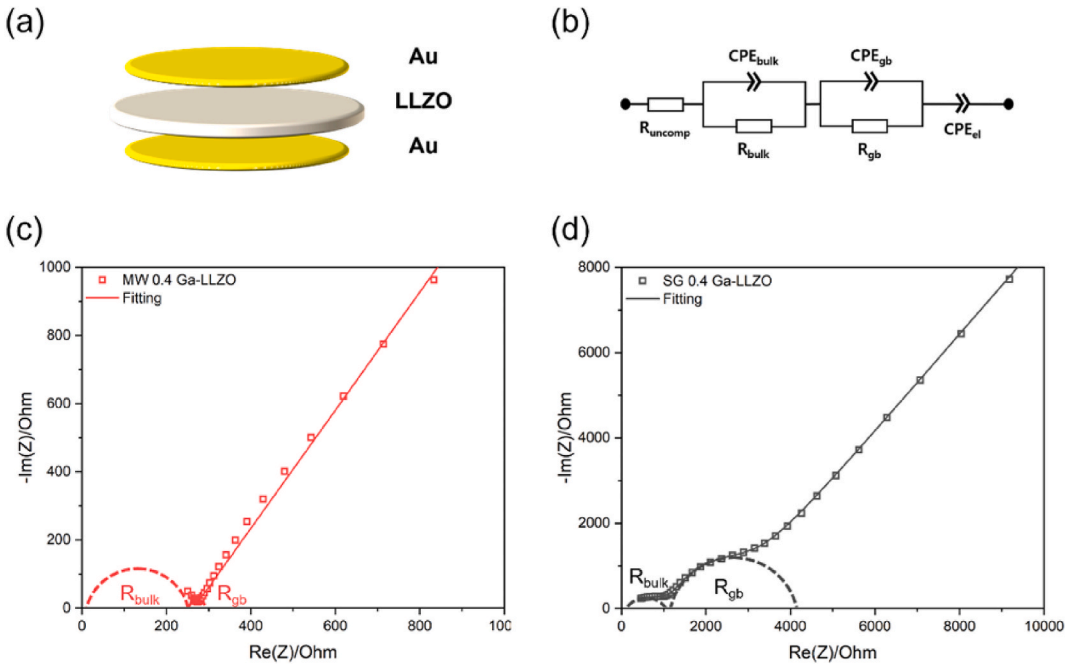

Fig. 6. (a) Schematic of the Au/Ga–LLZO/Au cell fabricated for EIS measurements; (b) equivalent circuit for fitting the EIS data of the Au/Ga–LLZO/Au cell; (c, d) Nyquist plots of (c) Au/MW 0.4 Ga–LLZO/Au and (d) Au/SG 0.4 Ga–LLZO/Au cells.

$$\sigma_{total} = \boldsymbol{A}\ \boldsymbol{exp}\left[\frac{-\boldsymbol{E_a}}{\boldsymbol{K_B T}}\right], \tag{2}$$

where A, k_B, and T represent the pre-exponential factor, Boltzmann's constant, and absolute temperature, respectively. The analysis reveals that the activation energy of the MW 0.2 Ga–LLZO, MW 0.3 Ga–LLZO, and MW 0.4 Ga–LLZO solid electrolytes are 0.38, 0.38, and 0.32 eV, respectively. Overall, Fig. 3d demonstrates a distinct relationship between Ga content and activation energy, indicating that a high Ga content results in low activation energies. However, as shown in Fig. S5, the activation energy increases when the Ga content exceeds 0.4 mol%. Small grains with high Ga contents exhibit over-coarsening during the subsequent sintering process and thus increase the activation energy. This abnormal grain growth reduces the driving force for sintering and increases the diffusion distance for mass transport, thereby slowing down sintering and limiting densification [49,56]. Furthermore, the pores trapped within the abnormal grains can induce a stress concentration, thereby decreasing the mechanical strength and ultimately causing the ceramic to fracture. These factors contribute to the lower ionic conductivity observed. Figs. S6 and S7 show the resistance, Li-ion conductivity, and activation energy as functions of the Ga content.

To determine the effect of the particle size of Ga–LLZO on grain formation and on its Li-ion conductivity during pellet sintering, MW 0.4 Ga–LLZO, i.e., the sample with the optimized Ga content (0.4 mol%) prepared using the MW-assisted method, was compared with 0.4 Ga–LLZO, which was synthesized by the conventional SG method (hereafter denoted by SG 0.4 Ga–LLZO). Fig. 4 shows the SEM images of the precursors, powders, and pellets (fracture surface) of MW 0.4 Ga–LLZO and SG 0.4 Ga–LLZO. The particle size of the SG 0.4 Ga–LLZO precursor powder (Fig. 4d, e and S8b) are larger than those of the MW 0.4 Ga–LLZO precursors (Fig. 4a and b, and S8a), whereas the morphology of the former is less uniform than that of the latter. The particle size distributions and surface area of MW 0.4 Ga–LLZO and SG 0.4 Ga–LLZO after calcination are presented in Figs. S9 and S10 and Table S1. The average particle sizes (d_{50}) of MW 0.4 Ga–LLZO and SG 0.4 Ga–LLZO are 0.80 and 14.28 μm, respectively, and their specific surface areas are 0.81 and 0.67 m^2/g, indicating that MW 0.4 Ga–LLZO has both smaller particles and a larger specific surface area. These characteristics can facilitate advantageous grain coarsening during sintering, which may increase the density and enhance Li-ion conductivity. In contrast, the SG 0.4 Ga–LLZO pellet does not undergo grain coarsening because of its microscale precursor powder particles, and it exhibits numerous grain boundaries, as shown in Fig. 4f.

To measure the grain boundaries inside each pellet with a high accuracy, samples were prepared by ion milling. Fig. 5 shows the SEM image and EDS data of the ion-milled pellet surface. The EDS analysis results indicate that SG 0.4 Ga–LLZO contains numerous grain boundaries and holes. In addition, the concentration of Ga in the form of $LiGaO_2$ was analyzed at the grain boundaries in SG 0.4 Ga–LLZO. $LiGaO_2$ forms at the grain boundaries because of the decreasing stability of Li metal [50,57]. The XRD pattern of SG 0.4 Ga–LLZO in Fig. S11 confirms the presence of $LiGaO_2$, which most likely formed at the grain boundaries as a consequence of the decreased stability of Li. Notably, as Li dendrites preferentially propagate along the grain boundaries and through interconnected holes, poorly sintered LLZO tends to form Li dendrites during the charge–discharge process.

Owing to the large amount of grain boundaries and holes, SG 0.4 Ga–LLZO can affect the Li-ion conductivity and performance of the

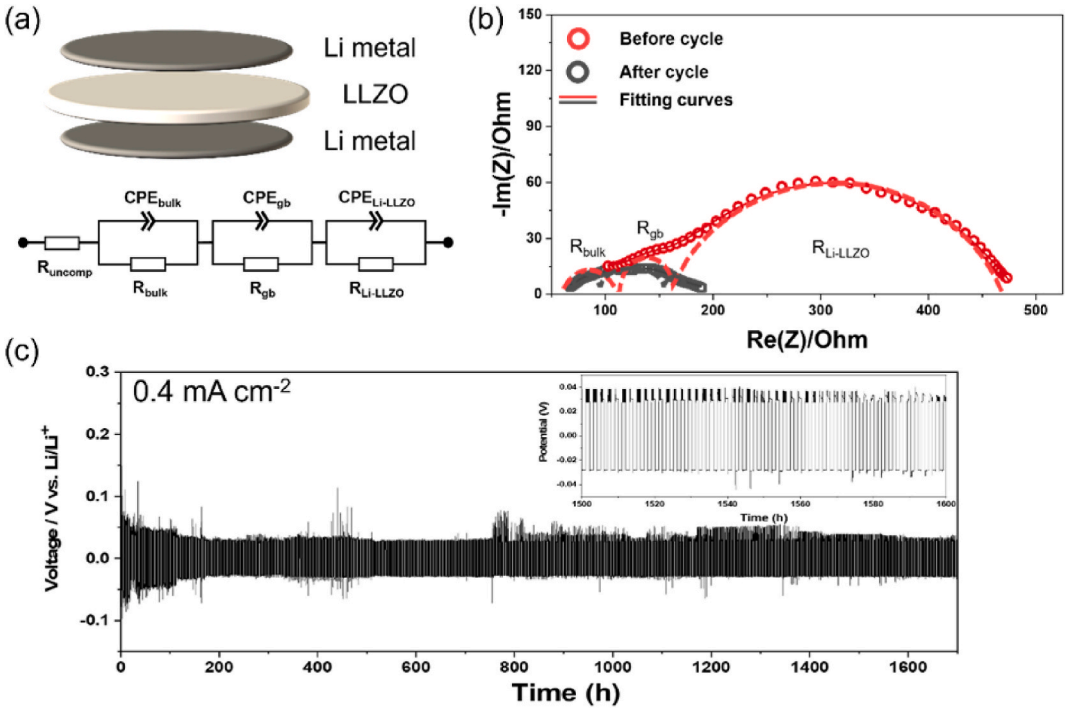

Fig. 7. (a) Schematic of the Li/MW 0.4 Ga–LLZO/Li cell and the equivalent circuit used to fit the EIS data. (b) Nyquist plots of the Li/MW 0.4 Ga–LLZO/Li cell before and after cycling. (c) Galvanostatic cycling of the Li/MW 0.4 Ga–LLZO/Li cell at 0.4 mA cm^{-2}.

associated battery. In contrast, MW 0.4 Ga–LLZO, which exhibits negligible grain boundaries and holes, can potentially mitigate such negative effects. In addition, a comparison of the EDS analysis results (Fig. 5c and f) reveals that Ga is more uniformly distributed throughout MW 0.4 Ga–LLZO than in the corresponding SG sample. The relative densities of the MW 0.4 Ga–LLZO and SG 0.4 Ga–LLZO pellets were 96 % and 91 %, respectively, as determined by the Archimedes method. The high relative density of the MW 0.4 Ga–LLZO pellet indicates its successful densification and minimized porosity, which could not be realized in the SG 0.4 Ga–LLZO pellet.

The Li-ion conductivities of the MW 0.4 Ga–LLZO and SG 0.4 Ga–LLZO pellets, determined by EIS, are compared in Fig. 6. The total resistances of the MW and SG 0.4 Ga–LLZO pellets are 265 and 2216 Ω, respectively. The calculated Li-ion conductivity of the SG 0.4 Ga–LLZO pellet is extremely low (only 1.13×10^{-4} S cm^{-1}), and thus, this solid electrolyte is not suitable for cell application.

Upon comparing the pellet morphologies in Figs. 4 and 5 and the EIS results in Fig. 6, we can conclude that the MW 0.4 Ga–LLZO pellet prepared from nanostructured Ga–LLZO shows low interfacial and grain-boundary resistivities and is thus expected to outperform SG 0.4 Ga–LLZO as a high-performance Li-ion solid electrolyte (Fig. S12).

3.3. *Cycling stability*

To examine the stability of the prepared MW 0.4 Ga–LLZO solid electrolyte upon contact with Li metal in LIBs, galvanostatic cycling was performed on a Li/MW 0.4 Ga–LLZO/Li symmetric cell at room temperature and a current density of 0.4 mA cm^{-2}; the corresponding results are shown in Fig. 7. The obtained EIS data were fitted with the equivalent circuit model shown in Fig. 7a to assess the resistance before and after the galvanostatic cycling test, and the fitted EIS results are presented in Fig. 7b. The initial cell configuration has a nonuniform interface that causes a high resistance. However, we observe that the resistance after 1600 h cycling is significantly lower than that before cycling. As shown in Table S2, the impedance values for each component indicate that R_b decreased from 76 to 46 Ω, and R_{gb} decreased from 94 to 81 Ω after cycling. Notably, the impedance of the entire Li/MW 0.4 Ga–LLZO/Li cell ($R_{Li-LLZO}$) significantly decreased from 302 to 49 Ω after cycling, indicating a substantial reduction in the Li/LLZO interfacial impedance. This suggests that the unstable interface between the Li metal and MW 0.4 Ga–LLZO, which initially exhibited only simple physical adhesion, was stabilized by electrodeposition after cycling.

Fig. 7c shows the time–voltage profile obtained by cycling for over 1700 h at room temperature at a constant current density of 0.4 mA cm^{-2}. The Li/MW 0.4 Ga–LLZO/Li cell is repeatedly charged and discharged for 1 h per cycle. In this profile, a positive voltage indicates Li stripping, whereas a negative voltage indicates Li electrodeposition. Although the voltage initially fluctuated, the results demonstrate the excellent reversibility of the Li redox reactions in the cell and the high stability of the MW 0.4 Ga–LLZO electrolyte over prolonged testing for approximately 1700 h.

4. Conclusions

In this study, we synthesized a low-resistance solid electrolyte using an MW-assisted solvothermal method. The solid electrolyte powders synthesized by this method were composed of nanostructured LLZO after calcination and facilitated high grain coarsening during sintering; thus, the number of grain boundaries was considerably reduced. Furthermore, the lowest resistance was observed at a Ga content of 0.4 mol%. An electrolyte with the optimized Ga content (0.4 mol%) was prepared by the SG method for comparison, which confirmed that the MW-assisted solvothermal method considerably reduced the number of grain boundaries in the final pellets. These MW-synthesized pellets exhibited a high Li-ion conductivity (1.04×10^{-3} S cm^{-1}) and a low activation energy (0.32 eV) at 25 °C. Furthermore, in the stability test with Li metal, the MW 0.4 Ga–LLZO pellets exhibited a lifespan of >1700 h during galvanostatic cycling at a high current density of 0.4 mA cm^{-2}. This study demonstrates the effectiveness of the MW-assisted solvothermal method as a new approach for synthesizing high-performance solid electrolytes.

Data availability statement

Data will be made available on request.

CRediT authorship contribution statement

Seong-Jun Jo: Writing – original draft, Investigation, Formal analysis, Data curation, Conceptualization. **Young Gyu Jeon:** Writing – original draft, Visualization, Investigation, Formal analysis, Data curation. **Dong-Kyu Kim:** Writing – original draft, Visualization, Methodology, Investigation, Formal analysis, Data curation. **Sang Yeop Hwang:** Writing – review & editing, Visualization, Formal analysis, Data curation. **Byeong-Heon Lee:** Formal analysis, Data curation. **Chea Yun Kang:** Data curation, Visualization, Writing – review & editing. **Seung-Hwan Lee:** Methodology, Formal analysis, Data curation, Writing – review & editing, Visualization. **Sung-Hwan Lim:** Methodology, Formal analysis, Data curation, Writing – review & editing, Visualization. **R. Vasant Kumar:** Writing – review & editing, Methodology, Formal analysis. **Yu-Jin Han:** Writing – review & editing, Writing – original draft, Supervision, Investigation, Data curation. **Kwang-Bum Kim:** Writing – review & editing, Writing – original draft, Supervision, Conceptualization. **Hyun-Kyung Kim:** Writing – review & editing, Writing – original draft, Visualization, Supervision, Project administration, Methodology, Investigation, Data curation, Conceptualization.

Declaration of competing interest

The authors declare that they have no known competing financial interests or personal relationships that could have appeared to influence the work reported in this paper.

Acknowledgments

This research was supported by the POSCO Science Fellowship from the POSCO TJ Park Foundation and the National Research Foundation of Korea (NRF) Grant funded by the Korea Government (MSIT; No. RS-2023-00277946). This work was also supported by the Technology Innovation Program (RS-2022-00155791) funded by the Ministry of Trade, Industry & Energy (MOTIE, Korea).

Appendix A. Supplementary data

Supplementary data to this article can be found online at https://doi.org/10.1016/j.heliyon.2024.e36206.

References

[1] J.M. Tarascon, M. Armand, Issues and challenges facing rechargeable lithium batteries, Nature 414 (2001) 359–367, https://doi.org/10.1038/35104644.
[2] V. Etacheri, R. Marom, R. Elazari, G. Salitra, D. Aurbach, Challenges in the development of advanced Li-ion batteries: a review, Energy Environ. Sci. 4 (2011) 3243–3262, https://doi.org/10.1039/c1ee01598b.
[3] H. Li, Z. Wang, L. Chen, X. Huang, Research on advanced materials for Li-ion batteries, Adv. Mater. 21 (2009) 4593–4607, https://doi.org/10.1002/adma.200901710.
[4] A.J. Samson, K. Hofstetter, S. Bag, V. Thangadurai, A bird's-eye view of Li-stuffed garnet-type Li 7 La 3 Zr 2 O 12 ceramic electrolytes for advanced all-solid-state Li batteries, Energy Environ. Sci. 12 (2019) 2957–2975, https://doi.org/10.1039/C9EE01548E.
[5] Q. Liu, Z. Geng, C. Han, Y. Fu, S. Li, Y.-b. He, F. Kang, B. Li, Challenges and perspectives of garnet solid electrolytes for all solid-state lithium batteries, J. Power Sources 389 (2018) 120–134, https://doi.org/10.1016/j.jpowsour.2018.04.019.
[6] B. Zhang, R. Tan, L. Yang, J. Zheng, K. Zhang, S. Mo, Z. Lin, F. Pan, Mechanisms and properties of ion-transport in inorganic solid electrolytes, Energy Storage Mater. 10 (2018) 139–159, https://doi.org/10.1016/j.ensm.2017.08.015.
[7] L. Zhu, T.-F. Yan, D. Jia, Y. Wang, Q. Wu, H.-T. Gu, Y.-M. Wu, W.-P. Tang, LiFePO4-coated LiNi0. 5Co0. 2Mn0, 3O2 cathode materials with improved high voltage electrochemical performance and enhanced safety for lithium ion pouch cells, J. Electrochem. Soc. 166 (2019) A5437–A5444. https://10.1149/2.0651903jes.
[8] Z.D. Li, Y.C. Zhang, H.F. Xiang, X.H. Ma, Q.F. Yuan, Q.S. Wang, C.H. Chen, Trimethyl phosphite as an electrolyte additive for high-voltage lithium-ion batteries using lithium-rich layered oxide cathode, J. Power Sources 240 (2013) 471–475, https://doi.org/10.1016/j.jpowsour.2013.04.038.

[9] K. Takada, Progress in solid electrolytes toward realizing solid-state lithium batteries, J. Power Sources 394 (2018) 74–85, https://doi.org/10.1016/j.jpowsour.2018.05.003.

[10] Q. Zhang, D. Cao, Y. Ma, A. Natan, P. Aurora, H. Zhu, Sulfide-based solid-state electrolytes: synthesis, stability, and potential for all-solid-state batteries, Adv. Mater. 31 (2019) e1901131, https://doi.org/10.1002/adma.201901131.

[11] J. Wolfenstine, J.L. Allen, J. Sakamoto, D.J. Siegel, H. Choe, Mechanical behavior of Li-ion-conducting crystalline oxide-based solid electrolytes: a brief review, Ionics 24 (2018) 1271–1276, https://doi.org/10.1007/s11581-017-2314-4.

[12] S. Yu, R.D. Schmidt, R. Garcia-Mendez, E. Herbert, N.J. Dudney, J.B. Wolfenstine, J. Sakamoto, D.J. Siegel, Elastic properties of the solid electrolyte Li7La3Zr2O12 (LLZO), Chem. Mater. 28 (2016) 197–206, https://doi.org/10.1021/acs.chemmater.5b03854.

[13] Y. Inaguma, C. Liquan, M. Itoh, T. Nakamura, T. Uchida, H. Ikuta, M. Wakihara, High ionic conductivity in lithium lanthanum titanate, Solid State Commun. 86 (1993) 689–693, https://doi.org/10.1016/0038-1098(93)90841-A.

[14] H. Aono, E. Sugimoto, Y. Sadaoka, N. Imanaka, G.y. Adachi, Ionic conductivity of solid electrolytes based on lithium titanium phosphate, J. Electrochem. Soc. 137 (1990) 1023–1027, https://doi.org/10.1149/1.2086597.

[15] R. Murugan, V. Thangadurai, W. Weppner, Fast lithium ion conduction in garnet-type Li7La3Zr2O12, Angew. Chem., Int. Ed. Engl. 46 (2007) 7778–7781, https://doi.org/10.1002/anie.200701144.

[16] C.A. Geiger, E. Alekseev, B. Lazic, M. Fisch, T. Armbruster, R. Langner, M. Fechtelkord, N. Kim, T. Pettke, W. Weppner, Crystal chemistry and stability of "Li7La3Zr2O12" garnet: a fast lithium-ion conductor, Inorg. Chem. 50 (2011) 1089–1097, https://doi.org/10.1021/ic101914e.

[17] Y. Zhu, X. He, Y. Mo, Origin of outstanding stability in the lithium solid electrolyte materials: insights from thermodynamic analyses based on first-principles calculations, ACS Appl. Mater. Interfaces 7 (2015) 23685–23693, https://doi.org/10.1021/acsami.5b07517.

[18] H. Chung, B. Kang, Mechanical and thermal failure induced by contact between a Li1. 5Al0. 5Ge1. 5, Chem. Mater. 29(20), PO4 3 solid electrolyte and Li metal in an all solid-state Li cell (2017) 8611–8619.

[19] S. Wenzel, T. Leichtweiss, D. Krüger, J. Sann, J. Janek, Interphase formation on lithium solid electrolytes—an in situ approach to study interfacial reactions by photoelectron spectroscopy, Solid State Ionics 278 (2015) 98–105, https://doi.org/10.1016/j.ssi.2015.06.001.

[20] P. Hartmann, T. Leichtweiss, M.R. Busche, M. Schneider, M. Reich, J. Sann, P. Adelhelm, J. Janek, Degradation of NASICON-type materials in contact with lithium metal: formation of mixed conducting interphases (MCI) on solid electrolytes, J. Phys. Chem. C 117 (2013) 21064–21074, https://doi.org/10.1021/jp4051275.

[21] M.M. Raju, F. Altayran, M. Johnson, D. Wang, Q. Zhang, Crystal structure and preparation of Li7La3Zr2O12 (LLZO) solid-state electrolyte and doping impacts on the conductivity: an overview, Electrochemistry (Tokyo, Jpn.) 2 (2021) 390–414.

[22] D. Wang, G. Zhong, W.K. Pang, Z. Guo, Y. Li, M.J. McDonald, R. Fu, J.-X. Mi, Y. Yang, Toward understanding the lithium transport mechanism in garnet-type solid electrolytes: Li+ ion exchanges and their mobility at octahedral/tetrahedral sites, Chem. Mater. 27 (2015) 6650–6659, https://doi.org/10.1021/acs.chemmater.5b02429.

[23] X. Huang, J. Su, Z. Song, T. Xiu, J. Jin, M.E. Badding, Z. Wen, Synthesis of Ga-doped Li7La3Zr2O12 solid electrolyte with high Li+ ion conductivity, Ceram. Int. 47 (2021) 2123–2130, https://doi.org/10.1016/j.ceramint.2020.09.047.

[24] X. Li, R. Li, S. Chu, K. Liao, R. Cai, W. Zhou, Z. Shao, Rational design of strontium antimony co-doped Li7La3Zr2O12 electrolyte membrane for solid-state lithium batteries, J. Alloys Compd. 794 (2019) 347–357, https://doi.org/10.1016/j.jallcom.2019.04.274.

[25] T. Thompson, J. Wolfenstine, J.L. Allen, M. Johannes, A. Huq, I.N. David, J. Sakamoto, Tetragonal vs. cubic phase stability in Al–free Ta doped Li 7 La, J. Mater. Chem. A 2 (33) (2014) 13431–13436, 3 Zr 2 O 12 (LLZO).

[26] C. Liu, K. Rui, C. Shen, M.E. Badding, G. Zhang, Z. Wen, Reversible ion exchange and structural stability of garnet-type Nb-doped Li7La3Zr2O12 in water for applications in lithium batteries, J. Power Sources 282 (2015) 286–293, https://doi.org/10.1016/j.jpowsour.2015.02.050.

[27] Y. Lu, X. Meng, J.A. Alonso, M.T. Fernández-Díaz, C. Sun, Effects of fluorine doping on structural and electrochemical properties of Li6. 25Ga0. 25La3Zr2O12 as electrolytes for solid-state lithium batteries, ACS Appl. Mater. Interfaces 11 (2019) 2042–2049, https://doi.org/10.1021/acsami.8b17656.

[28] S.R. Yeandel, B.J. Chapman, P.R. Slater, P. Goddard, Structure and lithium-ion dynamics in fluoride-doped cubic Li7La3Zr2O12 (LLZO) garnet for Li solid-state battery applications, J. Phys. Chem. C 122 (2018) 27811–27819, https://doi.org/10.1021/acs.jpcc.8b07704.

[29] S.M. Alizadeh, I. Moghim, M. Golmohammad, Synthesis and characterization of highly conductive Ga/Y co-doped LLZO by facile combustion sol-gel method, Solid State Ionics 397 (2023) 116260, https://doi.org/10.1016/j.ssi.2023.116260.

[30] O. Sharifi, M. Golmohammad, M. Soozandeh, A.S. Mehranjani, Improved Ga-doped Li7La3Zr2O12 garnet-type solid electrolytes for solid-state Li-ion batteries, J. Solid State Electrochem. 27 (2023) 2433–2444, https://doi.org/10.1007/s10008-023-05522-w.

[31] M. Golmohammad, A. Sazvar, M.M. Maleki Shahraki, M. Salimi, Effects of Nd and Al co-doping on the microstructure and lithium-ion transport in Li7La3Zr2O12 solid-state batteries, Solid State Ionics 412 (2024) 116598, https://doi.org/10.1016/j.ssi.2024.116598.

[32] M. Ashuri, M. Golmohammad, A. Soleimany Mehranjani, M. Faghihi Sani, Al-doped Li 7 La 3 Zr 2 O 12 garnet-type solid electrolytes for solid-state Li-Ion batteries, J. Mater. Sci. Mater. Electron. 32 (2021) 6369–6378, https://doi.org/10.1007/s10854-021-05353-3.

[33] R.H. Brugge, F.M. Pesci, A. Cavallaro, C. Sole, M.A. Isaacs, G. Kerherve, R.S. Weatherup, A. Aguadero, The origin of chemical inhomogeneity in garnet electrolytes and its impact on the electrochemical performance, J. Mater. Chem. A 8 (2020) 14265–14276, https://doi.org/10.1039/D0TA04974C.

[34] D. Huang, M. Kamiko, S. Yagi, Synthesis Conditions Affecting Electrochemical and Chemical Stabilities of Ga-Doped Li7La3Zr2O12 Solid Electrolyte, EcoEnergy, 2024, https://doi.org/10.1002/ece2.24.

[35] X. Xiang, Z. Fang, F. Chen, H. Wang, W. Yang, C. Wei, J. Yang, X. Ma, D. Chen, K. Sun, Y. Zhang, Q. Shen, Crystal structure of cubic Li7-3xGaxLa3Zr2O12 with space group of I-43d, Ceram. Int. 48 (2022) 9371–9377, https://doi.org/10.1016/j.ceramint.2021.12.132.

[36] Z.Z. Fang, H. Wang, Densification and grain growth during sintering of nanosized particles, Int. Mater. Rev. 53 (2008) 326–352, https://doi.org/10.1179/174328008X353538.

[37] R.M. German, Coarsening in sintering: grain shape distribution, grain size distribution, and grain growth kinetics in solid-pore systems, Crit. Rev. Solid State Mater. Sci. 35 (2010) 263–305, https://doi.org/10.1080/10408436.2010.525197.

[38] H.J. Kitchen, S.R. Vallance, J.L. Kennedy, N. Tapia-Ruiz, L. Carassiti, A. Harrison, A.G. Whittaker, T.D. Drysdale, S.W. Kingman, D.H. Gregory, Modern microwave methods in solid-state inorganic materials chemistry: from fundamentals to manufacturing, Chem. Rev. 114 (2014) 1170–1206, https://doi.org/10.1021/cr4002353.

[39] H. Zhang, F. Li, Q. Jia, G. Ye, Preparation of titanium carbide powders by sol-gel and microwave carbothermal reduction methods at low temperature, J. Sol. Gel Sci. Technol. 46 (2008) 217–222, https://doi.org/10.1007/s10971-008-1697-0.

[40] H. Yin, T. Yamamoto, Y. Wada, S. Yanagida, Large scale and size-controlled synthesis of silver nanoparticles under microwave irradiation, Mater. Chem. Phys. 83 (2004) 66–70, https://doi.org/10.1016/j.matchemphys.2003.09.006.

[41] J. Awaka, N. Kijima, H. Hayakawa, J. Akimoto, Synthesis and structure analysis of tetragonal Li7La3Zr2O12 with the garnet-related type structure, J. Solid State Chem. 182 (2009) 2046–2052, https://doi.org/10.1016/j.jssc.2009.05.020.

[42] J. Sakamoto, E. Rangasamy, H. Kim, Y. Kim, J. Wolfenstine, Synthesis of nano-scale fast ion conducting cubic Li7La3Zr2O12, Nanotechnology 24 (2013) 424005, https://doi.org/10.1088/0957-4484/24/42/424005.

[43] P.J. Kumar, K. Nishimura, M. Senna, A. Düvel, P. Heitjans, T. Kawaguchi, N. Sakamoto, N. Wakiya, H. Suzuki, A novel low-temperature solid-state route for nanostructured cubic garnet Li 7 La 3 Zr 2 O 12 and its application to Li-ion battery, RSC Adv. 6 (2016) 62656–62667, https://doi.org/10.1039/C6RA09695F.

[44] Z. Cao, W. Wu, Y. Li, J. Zhao, W. He, J. Liu, H. Zhang, G. Li, Lithium ionic conductivity of Li 7–3x Fe x La 3 Zr 2 O 12 ceramics by the Pechini method, Ionics 26 (2020) 4247–4256, https://doi.org/10.1007/s11581-020-03580-y.

[45] M. Kotobuki, K. Kanamura, Y. Sato, T. Yoshida, Fabrication of all-solid-state lithium battery with lithium metal anode using Al2O3-added Li7La3Zr2O12 solid electrolyte, J. Power Sources 196 (2011) 7750–7754, https://doi.org/10.1016/j.jpowsour.2011.04.047.

[46] C. Li, Y. Liu, J. He, K.S. Brinkman, Ga-substituted Li7La3Zr2O12: an investigation based on grain coarsening in garnet-type lithium ion conductors, J. Alloys Compd. 695 (2017) 3744–3752, https://doi.org/10.1016/j.jallcom.2016.11.277.

[47] J.-F. Wu, E.-Y. Chen, Y. Yu, L. Liu, Y. Wu, W.K. Pang, V.K. Peterson, X. Guo, Gallium-doped Li7La3Zr2O12 garnet-type electrolytes with high lithium-ion conductivity, ACS Appl. Mater. Interfaces 9 (2017) 1542–1552, https://doi.org/10.1021/acsami.6b13902.
[48] I. Kokal, M. Somer, P.H.L. Notten, H.T. Hintzen, Sol-gel synthesis and lithium ion conductivity of Li7La3Zr2O12 with garnet-related type structure, Solid State Ionics 185 (2011) 42–46, https://doi.org/10.1016/j.ssi.2011.01.002.
[49] Y. Tian, Y. Zhou, Y. Liu, C. Zhao, W. Wang, Y. Zhou, Formation mechanism of sol-gel synthesized Li7- 3xAlxLa3Zr2O12 and the influence of abnormal grain growth on ionic conductivity, Solid State Ionics 354 (2020) 115407, https://doi.org/10.1016/j.ssi.2020.115407.
[50] J. Li, H. Luo, K. Liu, J. Zhang, H. Zhai, X. Su, J. Wu, X. Tang, G. Tan, Excellent stability of Ga-doped garnet electrolyte against Li metal anode via eliminating LiGaO2 precipitates for advanced all-solid-state batteries, ACS Appl. Mater. Interfaces 15 (2023) 7165–7174, https://doi.org/10.1021/acsami.2c21603.
[51] P.H. Lee, S. Brahma, J. Dutta, J.-L. Huang, C.-P. Liu, Synergistic effects of Ga doping and Mg alloying over the enhancement of the stress sensitivity of a Ga-doped MgZnO pressure sensor, Nanoscale Adv. 3 (2021) 3909–3917, https://doi.org/10.1039/d0na01069c.
[52] X. Han, Y. Gong, K.K. Fu, X. He, G.T. Hitz, J. Dai, A. Pearse, B. Liu, H. Wang, G. Rubloff, Y. Mo, V. Thangadurai, E.D. Wachsman, L. Hu, Negating interfacial impedance in garnet-based solid-state Li metal batteries, Nat. Mater. 16 (2017) 572–579, https://doi.org/10.1038/nmat4821.
[53] J. Hüttl, C. Seidl, H. Auer, K. Nikolowski, A.L. Görne, M. Arnold, C. Heubner, M. Wolter, A. Michaelis, Ultra-low LPS/LLZO interfacial resistance–towards stable hybrid solid-state batteries with Li-metal anodes, Energy Storage Mater. 40 (2021) 259–267, https://doi.org/10.1016/j.ensm.2021.05.020.
[54] Y. Zhu, S. Wu, Y. Pan, X. Zhang, Z. Yan, Y. Xiang, Reduced energy barrier for Li+ transport across grain boundaries with amorphous domains in LLZO thin films, Nanoscale Res. Lett. 15 (2020) 153, https://doi.org/10.1186/s11671-020-03378-x.
[55] J. Li, K. Zhu, X. Zhang, T. Wang, X. Li, J. Wang, K. Yan, J. Liu, Effect of Ga-Bi co-doped on structural and ionic conductivity of Li 7 La 3 Zr 2 O 12 solid electrolytes derived from sol-gel method, J. Electron. Mater. 48 (2019) 7762–7768, https://doi.org/10.1007/s11664-019-07607-7.
[56] J. Su, X. Huang, Z. Song, T. Xiu, M.E. Badding, J. Jin, Z. Wen, Overcoming the abnormal grain growth in Ga-doped Li7La3Zr2O12 to enhance the electrochemical stability against Li metal, Ceram. Int. 45 (2019) 14991–14996, https://doi.org/10.1016/j.ceramint.2019.04.236.
[57] D. Kim, M.H. Nguyen, S.H. Chun, J. Jeon, B.-K. Kim, S. Park, Stabilization of Li7La3Zr2O12 solid electrolyte through Ga-based precipitates and the Ga–Au Surface Layer, Int. J. Energy Res. 2024 (2024) 1–15, https://doi.org/10.1155/2024/9050890.